# The Impact of SST Specification on ECMWF Surface Wind Stress Fields in the Eastern Tropical Pacific

DUDLEY B. CHELTON

*College of Oceanic and Atmospheric Sciences, Oregon State University, Corvallis, Oregon*

(Manuscript received 4 March 2004, in final form 10 August 2004)

ABSTRACT

The impact of SST specification on low-level winds in the operational ECMWF numerical weather prediction model is investigated in the eastern tropical Pacific from comparisons of ECMWF wind stress fields with QuikSCAT satellite scatterometer observations of wind stress during the August–December cold seasons of 2000 and 2001. These two time periods bracket the 9 May 2001 change from the Reynolds SST analyses to the Real-Time Global SST (RTG_SST) analyses as the ocean boundary condition in the ECMWF model. The ocean–atmosphere interaction in the eastern tropical Pacific that is clearly evident in QuikSCAT wind stress divergence and curl fields is also evident in the ECMWF winds, but is more than twice as strong in the 2001 cold season as in the 2000 cold season, due primarily to the improved spatial and temporal resolution of the RTG_SST analyses compared with the Reynolds SST analyses. While a significant improvement compared with 2000, the response of the 2001 ECMWF wind stress field to SST is only about half as strong as the coupling inferred from QuikSCAT data and satellite observations of SST from the Tropical Rainfall Measuring Mission (TRMM) Microwave Imager (TMI). It is concluded that the underrepresentation of the ocean–atmosphere coupling is attributable partly to underrepresentation of SST gradients in the RTG_SST fields and partly to inadequacies of the ECWMF model. The latter may be due to errors in the parameterization of boundary layer processes or to insufficient horizontal or vertical resolution in the model.

## 1. Introduction

Recent satellite observations demonstrating the remarkably strong influence of sea surface temperature (SST) on low-level winds have stimulated a resurgence of interest in ocean–atmosphere interaction near SST fronts throughout the World Ocean. This phenomenon was apparently first reported by Sweet et al. (1981) from aircraft observations of the marine atmospheric boundary layer (MABL) across the Gulf Stream. The same ocean–atmosphere interaction was observed by Jury and Walker (1988) from aircraft observations of the MABL across the Agulhas Current. Evidence for SST influence on low-level winds in the eastern tropical Pacific was presented by Wallace et al. (1989) based on climatological average ship observations and by Hayes et al. (1989) based on moored observations of SST and winds. The global coverage of satellite measurements of winds and SST reveals that this ocean–atmosphere coupling exists wherever there are strong SST fronts (Chelton et al. 2004; Xie 2004). The objective of this study is to determine the extent to which this SST influence on low-level winds is adequately represented in the eastern tropical Pacific by the European Centre for Medium-Range Weather Forecasts (ECMWF) numerical weather prediction model. This is assessed by investigating the sensitivity of the ECMWF wind stress fields to specification of the SST boundary condition.

This study was made possible by the 9 May 2001 implementation of a major change in the SST boundary condition in the ECMWF model. Prior to that time, the ocean boundary condition consisted of daily updates of weekly average SST analyses (referred to here as the "Reynolds SST analyses") produced operationally on a 1° global grid by the National Oceanic and Atmospheric Administration (NOAA; Reynolds and Smith 1994; Reynolds et al. 2002). On 30 January 2001, NOAA also began producing new operational high-resolution SST analyses that are referred to as the Real-Time Global SST (RTG_SST) fields (Thiébaux et al. 2003). The RTG_SST fields are provided as daily averages on a 0.5° global grid at daily intervals. The ocean boundary condition in the operational ECMWF model was changed to the RTG_SST analyses at 1800 UTC 9 May 2001. This change offers an opportunity to assess the impact of the specification of the SST

*Corresponding author address:* Dudley B. Chelton, College of Oceanic and Atmospheric Sciences, Oregon State University, 104 COAS Administration Building, Corvallis, OR 97331-5503.
E-mail: chelton@coas.oregonstate.edu

boundary condition on the ECMWF surface wind stress fields.[1]

The region considered in the present study is 5°S–5°N, 140°–95°W in the eastern tropical Pacific, which is almost identical to the Niño-3 region[2] for which the average SST is often used as an index of the El Niño–Southern Oscillation (ENSO) phenomenon. An important oceanographic feature of this region is the well-known equatorial cold tongue that is present during normal and La Niña years and becomes weak or nonexistent during El Niño years. Inadequate representation of the effects of the cold tongue on the ocean–atmosphere heat flux and the overlying wind field, and the associated feedback of the resulting surface wind stress perturbations on the ocean, may partly account for the conclusion by Mechoso et al. (1995) that coupled ocean–atmosphere models are unable to reproduce the observed structure of the cold tongue.

The eastern tropical Pacific is also the region where the ocean–atmosphere interaction process that is of interest here has received the greatest attention both from in situ studies (Wallace et al. 1989; Hayes et al. 1989; Bond 1992; Thum et al. 2002; Hashizume et al. 2002) and from satellite studies (Deser et al. 1993; Xie et al. 1998; Liu et al. 2000; Chelton et al. 2001; Hashizume et al. 2001). The SST fronts associated with the Pacific equatorial cold tongue are among the strongest in the World Ocean. During normal conditions, the surface wind stress from the cross-equatorial flow of the southeast trade winds decreases by more than a factor of 2 as air parcels are advected from warm to cold water across the south side of the cold tongue. The wind stress then increases by nearly the same amount as air parcels are advected from cold to warm water across the northern flank of the cold tongue.

The influence of SST on low-level winds in the eastern tropical Pacific is generally strongest during the August–December time period when the cold tongue is most well developed. As shown in Fig. 1, the geographical structures of the average SST field during this 5-month "cold season" were very similar in the year preceding and the year following the May 2001 change in the SST boundary condition in the ECMWF model. Other changes in the ECMWF model over the course of the August 2000–December 2001 time period analyzed here may have had some influence on the differences shown in section 5 between the surface wind stress fields during the 2000 and 2001 cold seasons. The most significant of these was an increase in the model grid resolution from T319 to T511 (i.e., from 0.564° to 0.352°) on 21 November 2000. It is argued in section 5 that the change in the SST boundary condition likely had the greatest impact on the modeling of SST-induced perturbations of low-level winds that are of interest in this study.

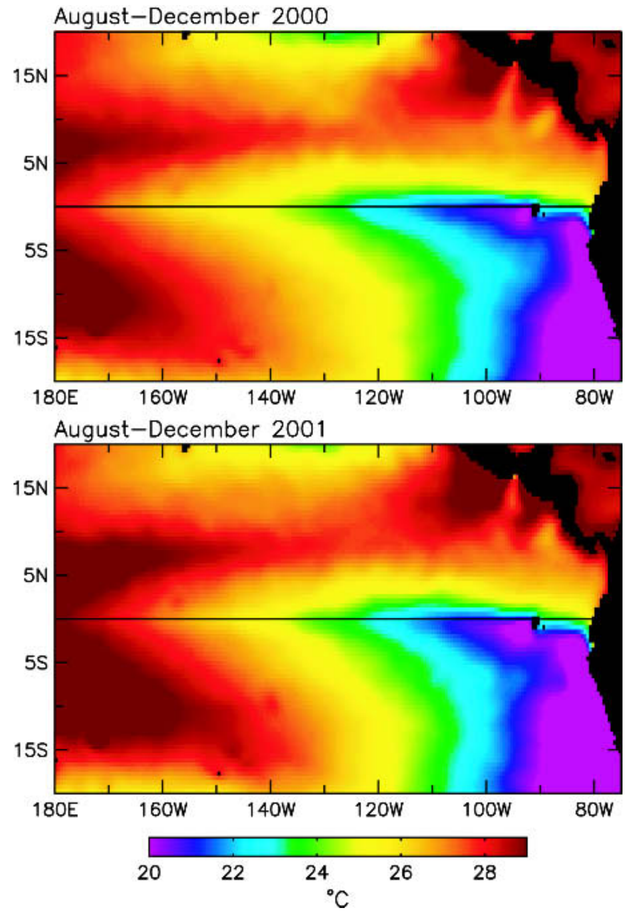


FIG. 1. Five-month averages of SST in the eastern tropical Pacific measured by the TMI for the Aug–Dec "cold seasons" of (top) 2000 and (bottom) 2001.

For the statistical analysis presented here, another important feature of the SST field in the eastern tropical Pacific is the existence of westward-propagating tropical instability waves (TIWs) that have wavelengths of 1000–2000 km, periods of 20–30 days, and phase speeds of about 0.5 m $s^{-1}$ (Qiao and Weisberg 1995). These characteristics of TIWs increase the number of independent realizations of the SST-induced perturbations of the wind field by creating varying locations, orientations, and intensities of SST fronts within the study region, thus improving the statistical reliability of the empirical relationships derived here between the winds and SST. The propagation characteristics of TIWs provide unambiguous evidence of the influence of SST on low-level winds.

TIWs are identifiable as cusplike distortions of the SST front along the northern flank of the equatorial cold tongue (Fig. 2). Similar, though weaker, features are present on the south side of the cold tongue (Chel-

[1] The National Centers for Environmental Prediction (NCEP) operational weather forecast model presently continues to use the Reynolds analyses as the SST boundary condition (B. Katz 2003, personal communication).

[2] The Niño-3 region is defined as 5°S–5°N, 150°–90°W.

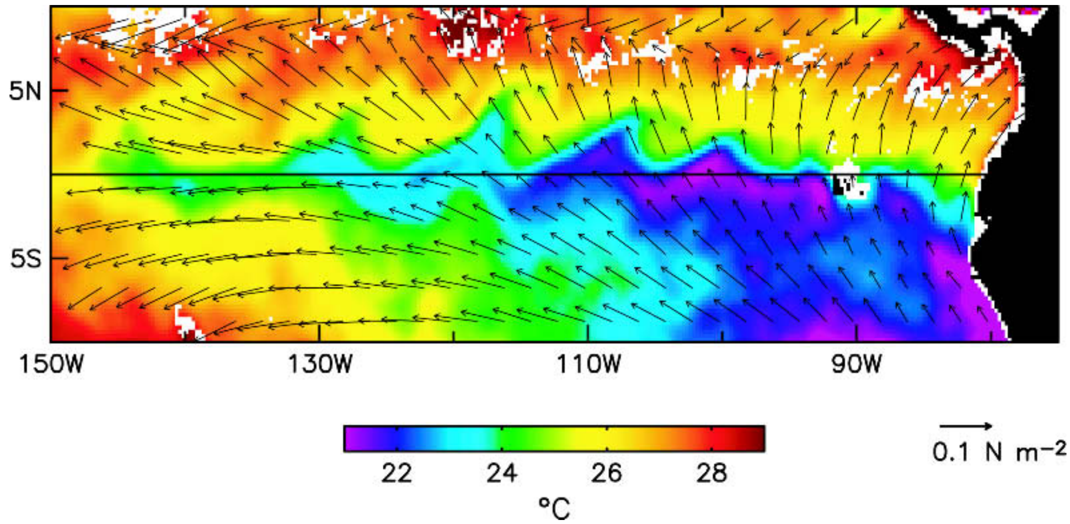


FIG. 2. The average SST measured by TMI over the 3-day time period 11–13 Dec 2001. The SST field was smoothed with a 2° by 2° loess smoother to remove small-scale noise from sampling errors in the short 3-day average. The vectors overlaid on the SST field are the QuikSCAT wind stresses on 12 December 2001, spatially and temporally smoothed as described in section 3c. For clarity, the QuikSCAT stress vectors are displayed on a 2° grid. The white areas and missing wind stress vectors represent missing TMI or QuikSCAT data owing to persistent rain contamination during the 3-day averaging period or to land contamination in the antenna side lobes.

ton et al. 2000, 2001). From time–longitude plots (left panel in Fig. 3), the SST signatures of TIWs were qualitatively similar during the August–December cold seasons of 2000 and 2001. In comparison, TIWs were much more energetic during the La Niña conditions of 1999 and they did not propagate as far west during the moderate El Niño conditions of 2002. To isolate the impact of the SST boundary condition on ECMWF wind stress fields, it is preferable to analyze years for which the oceanographic conditions are similar. The 2000 and 2001 cold seasons that bracket the May 2001 change of the SST boundary condition are therefore fortuitously well suited to the present study. The adequacy of the ECMWF model representation of the response of low-level winds to SST is evaluated here based on comparisons of ECMWF wind stress fields with wind stress fields constructed from QuikSCAT scatterometer data. Both of the time periods analyzed in this study predate the 22 January 2002 initiation of assimilation of QuikSCAT data into the ECMWF model.

The physical mechanisms underlying the observed ocean–atmosphere coupling near SST fronts are briefly reviewed in section 2. The SST and wind stress fields analyzed here and the filtering applied to these datasets are described in section 3. The spatial resolutions of the Reynolds and RTG_SST analyses of SST are assessed in section 4 from comparisons with satellite measurements of SST by the Tropical Rainfall Measuring Mission (TRMM) Microwave Imager (TMI). The ECMWF representations of SST-induced perturbations of wind stress before and after the May 2001 change of the model SST boundary condition are assessed in section 5. The paper concludes in section 6 with a summary of the results and a discussion of their implications for climatological average ECMWF wind stress fields in the eastern tropical Pacific.

## 2. SST-induced modification of low-level winds

The dynamics and thermodynamics of the observed relationship between SST and low-level winds are not completely understood. Sweet et al. (1981) and Wallace et al. (1989) suggested that the primary mechanism is the influence of SST on the stability of the MABL. In this scenario, atmospheric cooling over cool water increases stratification and stabilizes the MABL, inhibiting vertical mixing by turbulence and convection. This decouples the surface winds from the winds aloft and increases the wind shear near the sea surface, resulting in a decrease in the wind stress at the sea surface. Atmospheric heating over warm water decreases stratification and destabilizes the MABL, enhancing vertical turbulent mixing and deepening the MABL. This mixes momentum downward from aloft and decreases the wind shear near the sea surface, resulting in an increase in the wind stress at the sea surface. These effects of SST on low-level winds are shown schematically in Fig. S5 of Chelton et al. (2004) and are well represented in the large-eddy simulation (LES) modeling study by de Szoeke and Bretherton (2004). The hypothesized deepening of the MABL over warm water has been observed directly (Bond 1992; Jury 1994; Hashizume et al. 2002) and inferred from satellite measurements of increased low-level cloudiness (Deser et al. 1993; Hashizume et al. 2001; Xie et al. 2001).

It has also been suggested that the low-level wind

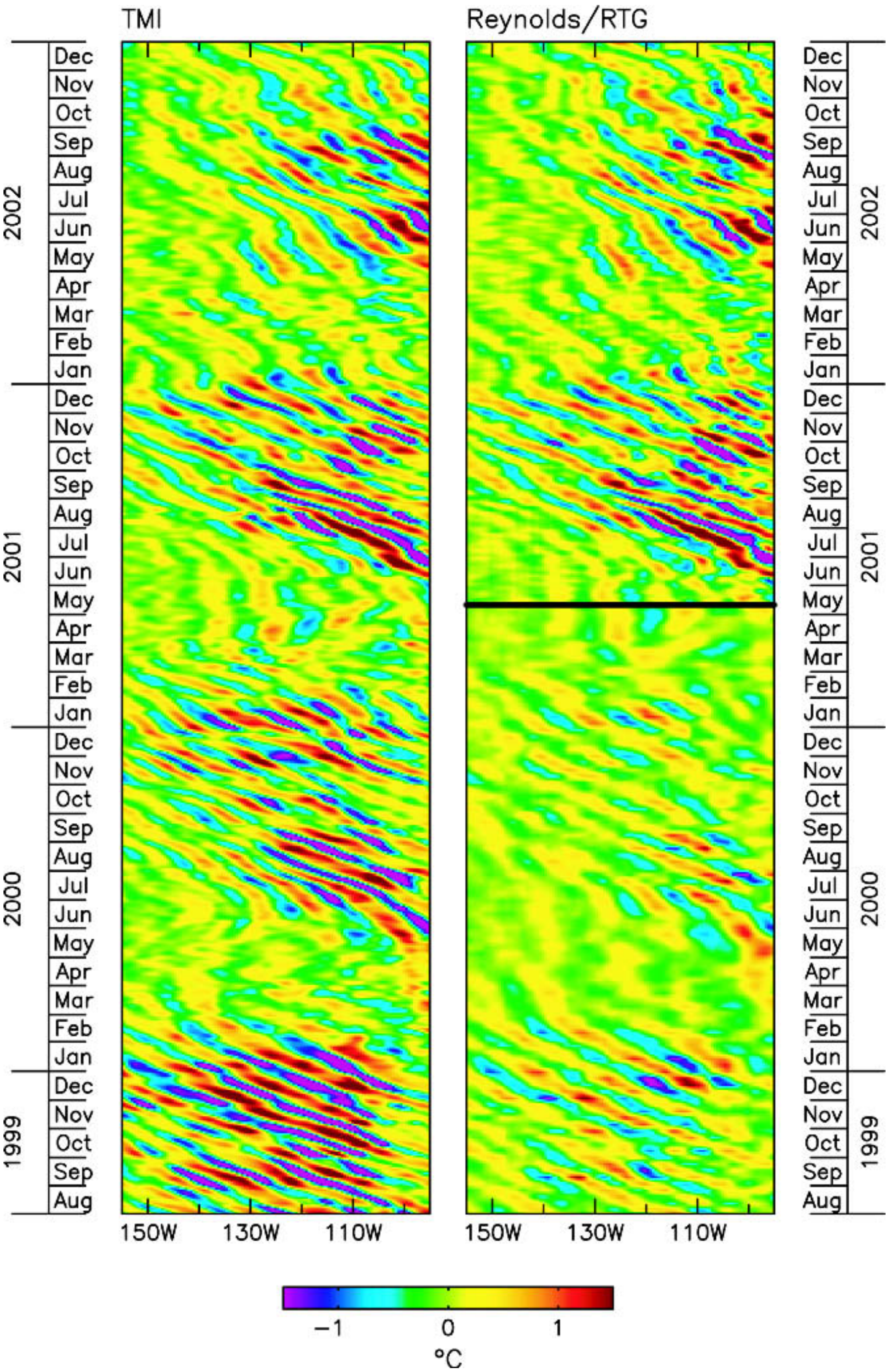


FIG. 3. Time–longitude plots of zonal high-pass-filtered SST along 2°N in the eastern tropical Pacific for the 3.5-yr time period Aug 1999–Dec 2002. (left) TMI measurements; (right) Reynolds analyses (prior to 9 May 2001) and RTG_SST analyses (after 9 May 2001) of SST. The SST fields from which these time–longitude plots were constructed were processed as described in section 3c.

response to SST is driven by cross-frontal pressure gradients (Lindzen and Nigam 1987). In this scenario, horizontal variations in the heating and cooling of the MABL create an enhanced pressure gradient force in the direction of the SST gradient. Observational evidence for this pressure gradient effect has been presented by Cronin et al. (2003). The modeling study by Small et al. (2003) provides additional evidence for the

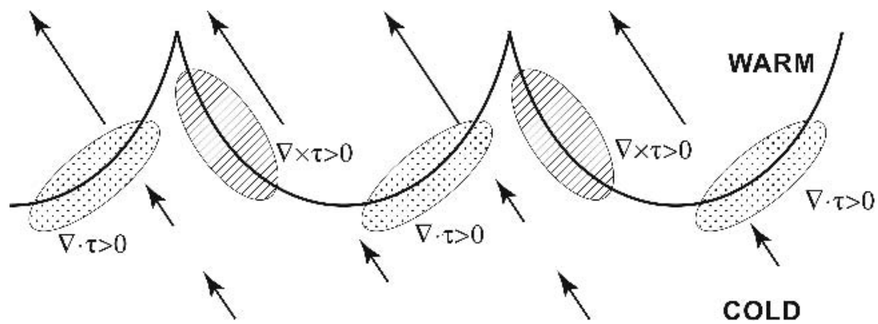


FIG. 4. A schematic summary of the SST influence on low-level winds in the eastern tropical Pacific. The southeast trade winds blow across the cusplike SST front on the north side of the cold tongue, represented here by the heavy black line. The wind stress magnitudes, represented by the lengths of the vectors, are relatively weak over the cold tongue and strong over the warmer water to the north. The wind stress divergence is strongest where the winds blow perpendicular to isotherms (i.e., parallel to the SST gradient), shown here as the stippled areas. The wind stress curl is strongest where the winds blow parallel to isotherms (i.e., perpendicular to the SST gradient), shown here as the hatched areas.

possible importance of pressure forcing. Small imbalances between the pressure gradient force and frictional effects from vertical turbulent mixing would accelerate the flow in regions of strong downwind SST gradients, resulting in higher surface wind speeds over warm water and lower surface wind speeds over cool water.

Regardless of the relative importance of SST-induced vertical turbulent mixing and cross-frontal pressure gradients, the observations unambiguously indicate that low-level winds are significantly altered near strong SST fronts. The net effects of SST on the MABL are to decrease the surface wind speed over cool water and increase it over warm water. As shown schematically in Fig. 4, the low-level wind response to spatial variations of the SST field near SST fronts is clearly identified from the divergence and curl of the wind stress field. Accelerations in regions where the winds blow across the distorted isotherms (stippled areas) lead to wind stress divergence. Lateral variations in regions where the winds blow parallel to the distorted isotherms (hatched areas) generate wind stress curl.

The geographical locations of maximum divergence and curl idealized in Fig. 4 are confirmed from the QuikSCAT observations (left panels in Fig. 5; see also Chelton et al. 2001). Between the equator and 5°N and about 90° and 120°W, the divergence is locally most intense on the west flank of each northward-pointing cusp in the SST front where the southeasterly winds blow across isotherms. Likewise, the curl within this

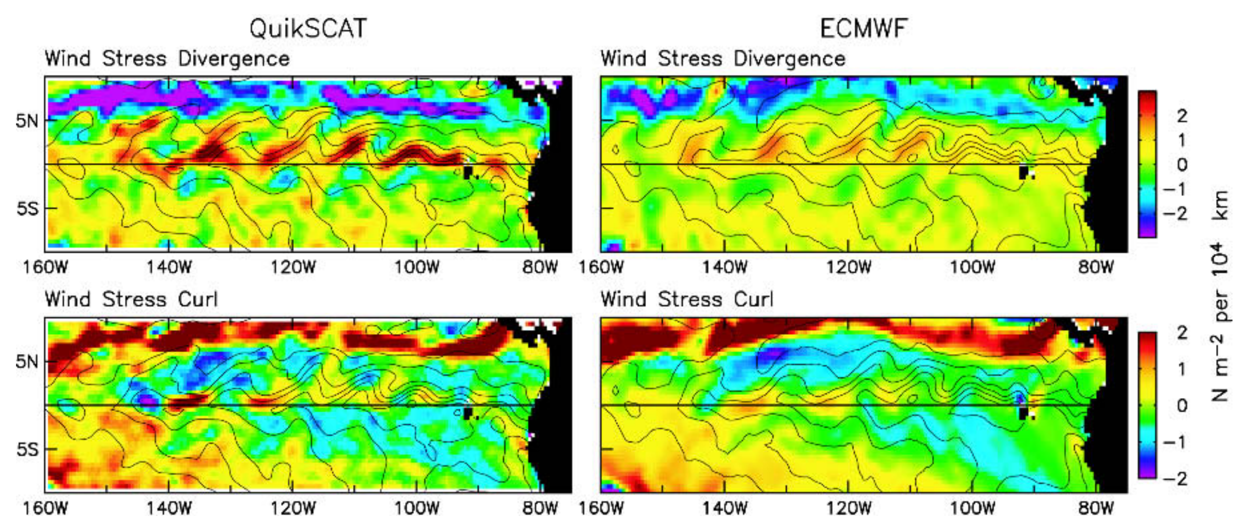


FIG. 5. Maps of the (top) wind stress divergence and (bottom) curl computed from (left) QuikSCAT observations and (right) ECMWF wind stress fields centered on 12 Dec 2001. The contours are SST from the (left) TMI and (right) RTG_SST fields centered on the same date. The wind stress curl and divergence fields and the SST fields were all processed as described in section 3c.

region is locally most intense on the east flank of each northward-pointing cusp and at lower latitudes where the winds blow parallel to isotherms. (The bands of strong convergence and positive curl north of 5°N associated with the intertropical convergence zone are unrelated to the SST influence of interest in this study.) To the west of about 120°W, the winds become more easterly (Fig. 2) and the geographical locations of the divergence and curl maxima shift accordingly in relation to the cusplike distortions of the SST front. The SST-induced perturbations of the divergence and curl are linearly related to the downwind and crosswind SST gradients, respectively (Chelton et al. 2001; O'Neill et al. 2003; O'Neill et al. 2004, manuscript submitted to the *Journal of Climate*; Chelton et al. 2004; see also section 5).

SST-induced perturbations of the low-level wind field are also evident in the ECMWF wind stress divergence and curl fields (right panels in Fig. 5), but with about half the magnitude of the QuikSCAT perturbations. These differences are quantified in section 5.

## 3. Data and filtering

### *a. Wind stress*

The response of the eastern tropical Pacific wind stress field to SST is quantified here from QuikSCAT observations of wind stress. The SeaWinds scatterometer on the QuikSCAT satellite is a scanning microwave radar that infers surface wind stress magnitude and direction with a resolution of about 25 km from the radar backscatter from the sea surface at multiple azimuth angles (Chelton and Freilich 2005). Scatterometer wind estimates are provided as the equivalent neutral stability wind vector that would be associated with the observed wind stress if the atmospheric boundary layer were neutrally stratified. The QuikSCAT equivalent neutral stability winds are based on the modified Large and Pond formulation of the drag coefficient (Trenberth et al. 1990).

The accuracy of the QuikSCAT equivalent neutral stability wind retrievals is estimated to be about 0.75 m $s^{-1}$ in the along-wind component and 1.5 m $s^{-1}$ in the crosswind component (Chelton and Freilich 2005). The wind speed accuracy is thus about 1.7 m $s^{-1}$ at all wind speeds. The directional accuracy is a sensitive function of wind speed at low wind speeds but improves rapidly with increasing wind speed. For 7 m $s^{-1}$ winds, the QuikSCAT wind direction accuracy is about 12°. Wind stress is obtained from these equivalent neutral stability winds using the same modified Large and Pond drag coefficient for neutral conditions, thus inverting the relation between wind and wind stress that is used in the calibration of the QuikSCAT wind retrievals.

The accuracies of ECMWF model simulations of the wind stress response to SST before and after the 9 May 2001 change of the SST boundary condition are assessed here from the ECMWF numerical weather prediction model forecast stresses for each 6-h synoptic period. [The ECMWF wind stress fields analyzed here were obtained from the ds111.3 data files archived at the National Center for Atmospheric Research (http://dss.ucar.edu/datasets/ds111.3)]. While the ECMWF model had computational grid resolutions of 0.564° and 0.352° before and after 21 November 2000, respectively, these wind stress fields were archived on a 1.125° Gaussian grid at 6-h intervals. The stresses at each grid point were available as the "accumulated stress" over each 6-h integration period, that is, the integral of the wind stress. The wind stress was obtained by dividing each accumulated stress by the 6-h time interval.

When compared with wind stress fields constructed from QuikSCAT data, the ECMWF forecast stress fields analyzed here were found to be more accurate than wind stress fields computed from the 6-hourly ECMWF analyses of 10-m winds using one of the usual wind speed–dependent formulations of the drag coefficient (e.g., Trenberth et al. 1990). Globally, the stresses computed from the ECMWF-accumulated forecast stresses were unbiased relative to the stresses computed from the QuikSCAT data. The ECMWF 10-m wind analyses are apparently biased low over most of the ocean by approximately 0.5 m $s^{-1}$ relative to buoy and QuikSCAT observations (Chelton and Freilich 2005). This corresponds to an underestimate of the wind stress by more than 10% over most of the World Ocean. The bias in the ECMWF 10-m wind analyses and the lack of bias in the ECMWF forecast stress fields have been confirmed from an independent analysis by H. Hersbach (2003, personal communication) at ECMWF.

### *b. Sea surface temperature*

The influence of SST on the wind stress field in the eastern tropical Pacific is assessed here from satellite microwave observations of SST by the TMI (Wentz et al. 2000; Chelton et al. 2000). At the frequencies relevant to SST estimation, the atmosphere is nearly transparent to microwave radiation in nonraining conditions. Rain-contaminated observations are easily identified and eliminated from the TMI dataset. TMI affords far greater data coverage compared with the traditional satellite infrared observations of SST, which are available only in cloud-free conditions (see Plate 1 of Chelton et al. 2000). The 46-km spatial resolution of TMI measurements compared with the 1-km resolution obtainable from infrared measurements is not a limiting factor for the present study. The accuracy of individual TMI SST estimates is about 0.6°C (Wentz et al. 2000; Gentemann et al. 2004). The smoothing described in section 3c substantially reduces the random component of the TMI measurement errors.

For the August–December 2000 analysis period, the SST boundary condition in the ECMWF model consisted of the Reynolds analyses of weekly average SST updated at daily intervals. These daily updates of 7-day-averaged SST are not as readily available as the weekly updates that are provided online by NOAA. The latter are therefore utilized in this study. This is not a serious limitation since all of the other SST and wind stress fields analyzed here were smoothed temporally, as summarized in section 3c, to attenuate variability with periods longer than 8 days.

The Reynolds SST analyses are computed by nonlinear iterative objective analysis (OA) on a 1° grid from a blending of ship, buoy, and satellite infrared measurements of SST (Reynolds and Smith 1994; Reynolds et al. 2002). The satellite data are adjusted to remove large-scale biases. Each weekly average SST analysis is based on a first guess that consists of the previous weekly average SST analysis adjusted by the climatological seasonal cycle. For consistency in data-sparse regions, correlation length scales of approximately 900 km zonally and 600 km meridionally are used in the Reynolds OA scheme in order to attenuate poorly resolved small-scale variability in the SST field. These long correlation scales impose large-scale spatial smoothing on the Reynolds SST analyses.

The weekly average Reynolds SST analyses produced at daily and weekly intervals for the same 7-day time period are not identical (Reynolds and Smith 1994). For present purposes, the differences are minor with one important exception: the time stamp on each daily analysis is 3.5 days later than the midpoint of the 7-day analysis period. Thus, for example, the time stamp on the daily analysis of the 7-day-averaged SST for the period 1–7 January is 0000 UTC on 8 January. For the same 7-day averaging period, the time stamp for the weekly Reynolds analyses utilized in this study would be 3.5 days earlier at 1200 UTC on 4 January, that is, the midpoint of the 7-day averaging period. Each daily analysis of 7-day-averaged SST was used as the ECMWF ocean boundary condition for the subsequent 24-h period. The SST boundary condition in the ECMWF model prior to 9 May 2001 thus consisted of the 7-day-averaged SST for times ranging from 3.5 to 4.5 days earlier than the actual SST conditions at each time step in the ECMWF model.

For the August–December 2001 analysis period, the SST boundary condition in the ECMWF model consisted of the Real-Time Global daily analyses of daily average SST (RTG_SST). The RTG_SST fields are computed on a 0.5° grid from a variational analysis that blends ship, buoy, and satellite infrared measurements of SST (Thiébaux et al. 2003). Large-scale biases in the satellite data are removed by the same method used in the Reynolds analyses. Each daily analysis is based on all of the ship, buoy, and satellite reports received during the 24-h period prior to the analysis run, with a maximum of 36 h of elapsed time since the observation. The time stamp on each daily RTG_SST field is 0000 UTC at the end of the 24-h analysis period. For the analysis presented here, these time stamps were adjusted backward by 12 h to 1200 UTC, which corresponds to the center of the 24-h analysis period. Each daily RTG_SST analysis of daily average SST was used as the ECMWF ocean boundary condition for the subsequent 24-h period. The SST boundary condition in the ECMWF model after 9 May 2001 thus consisted of the 24-h-averaged SST for times ranging from 0.5 to 1.5 days earlier than the actual SST conditions at each time step in the ECMWF model.

The ship, buoy and satellite data for the RTG_SST analyses are the same as those used in the Reynolds analyses. The primary difference between the two analysis schemes is in the specification of the length scales of the Gaussian correlation function used in the OA procedures. The Reynolds analyses are based on the previously noted anisotropic correlation length scales of about 900 km zonally and 600 km meridionally (Reynolds and Smith 1994). The RTG_SST analyses are based on isotropic correlation length scales that are inversely proportional to the magnitude of the climatological SST gradient magnitude. This inhomogeneous length scale ranges from 100 km for regions of strong SST gradients, such as the northern flank of the eastern equatorial Pacific cold tongue, to 450 km for regions of weak SST gradients (Thiébaux et al. 2003).

The RTG_SST analysis system was modified on 23 April 2002 to include a small amount of spatial smoothing of the daily SST fields to reduce small-scale noise attributed to 2-delta grid length waves arising from round-off error in the RTG_SST analyses (B. Katz 2003, personal communication). This smoothing postdates the August–December 2001 time period analyzed here. For the present analysis, this noise was mitigated by temporally smoothing the RTG_SST fields as described in section 3c.

### c. Filtering

Except for the SST fields in Figs. 2, 6, and 7, for which the highest possible resolution was desired, the datasets analyzed throughout this study were filtered as described in this section. The filtering parameters were carefully selected to attenuate short-time-scale weather variability and large spatial scale variability associated with the seasonal cycle, thereby highlighting the TIW-related ocean–atmosphere interaction that is the focus of this study.

The wind stress fields constructed from the 6-hourly ECMWF-accumulated forecast stresses were averaged over 1-day intervals centered at 1200 UTC on each day and spatially interpolated onto a 0.5° grid. These wind stress fields were then smoothed temporally with a loess smoother (Cleveland and Devlin 1988; Schlax et al. 2001) with a half-power filter cutoff period of 8 days. Wind stress curl and divergence were calculated from the unfiltered ECMWF 1.125° gridded fields by centered first differences and were then interpolated and temporally smoothed in the same manner as the ECMWF stresses. No spatial smoothing was applied to the inherently smooth ECMWF wind stress, divergence, or curl fields.

QuikSCAT wind stress fields were constructed on the same 0.5° grid and 1-day intervals as the ECMWF wind stress fields using a loess smoother with half-power filter cutoff wavelengths of 2° latitude by 4° longitude by 8 days. Wind stress divergence and curl fields were then computed from these 0.5° gridded and smoothed QuikSCAT wind stress fields by centered first differences.

No temporal or spatial smoothing was applied to the Reynolds weekly average SST fields. The half-power point of the filter transfer function for 7-day block averages is about 12 days (see Fig. 1 of Chelton and Schlax 2003). Because the Reynolds analyses are only produced as 7-day averages, 12-day variability is the highest periodicity that can be resolved in either the daily updates used in the ECMWF model or the weekly updates analyzed here. The weekly 1° gridded Reynolds SST fields were linearly interpolated onto the same 0.5° grid and 1-day intervals as all of the other datasets analyzed here.

The 0.5° gridded RTG_SST fields were temporally smoothed with the same 8-day loess smoothing that was applied to the TMI SST fields and to the QuikSCAT and ECMWF wind stress fields. No spatial smoothing was applied to the RTG_SST fields. The TMI observations of SST were smoothed and gridded in the same manner as the QuikSCAT data.

For Fig. 3 and the statistical analyses presented in sections 4 and 5, all of the wind stress and SST fields were zonally high-pass filtered to attenuate variability with zonal scales longer than 50° of longitude. This removes the large-scale variability that is well represented by all of the datasets, thus highlighting the TIW signals from which the rapid adjustment of the low-level wind field to SST is readily apparent. The TIW-induced perturbations of the SST and wind stress fields

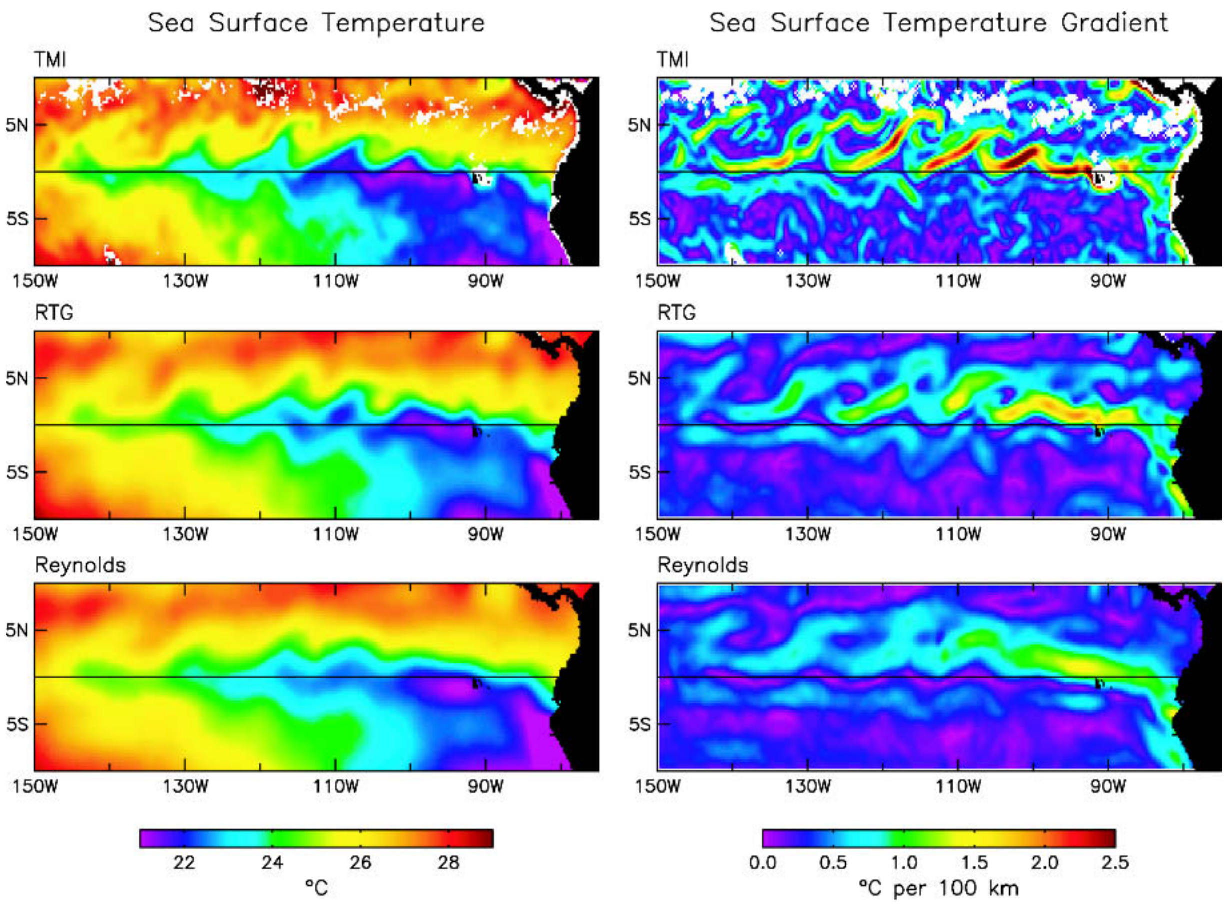


Fig. 6. Maps of (left) SST and (right) SST gradient magnitude constructed from (top) TMI observations, (middle) RTG_SST analyses, and (bottom) Reynolds analyses. For this figure, the TMI and RTG_SST fields were averaged over the 3-day time period 11–13 Dec 2001 and the Reynolds SST field is the weekly average centered on 12 Dec 2001. For display purposes, all of these SST fields were smoothed with a 2° × 2° loess smoother. This had little effect on the RTG_SST or Reynolds SST fields but reduced small-scale noise (which was amplified by the derivative operations in the SST gradient field) from sampling errors in the short 3-day average TMI SST field. As in Fig. 2, the white areas in the top panels represent missing TMI data owing to persistent rain contamination over the 3-day averaging period or to land contamination in the antenna side lobes.

isolated by the filtering applied here are referred to hereafter as the perturbation fields.

## 4. SST comparisons

Westward propagation is clearly present in time–longitude plots of the perturbation SST fields constructed from all three SST datasets (Fig. 3). Because of the spatial and temporal smoothing in the Reynolds analysis procedure, the dynamic range of TIW-induced perturbations of the SST front are much weaker in the Reynolds SST fields (lower-right half in Fig. 3) than in either the RTG_SST fields (upper-right half in Fig. 3) or the TMI SST fields (left panel in Fig. 3). It can be anticipated that the SST-induced perturbations of the ECMWF wind stress fields were much weaker prior to the 9 May 2001 change from the Reynolds analyses to the RTG_SST analyses for the ocean boundary condition. This is confirmed in section 5.

The smoothness of the Reynolds SST fields compared with the TMI and RTG_SST fields is evident in the representative example maps of SST and SST gradient for 12 December 2001 shown in Fig. 6. The Reynolds weekly average SST field centered on this date (bottom-left panel) captures the salient features of the undulating SST fronts on both sides of the cold tongue, but the sharp cusplike structures of these fronts are heavily smoothed. This smoothing is especially apparent in the SST gradient fields (bottom-right panel in Fig. 6).

The time–longitude characteristics of SST in the RTG_SST fields (upper-right half in Fig. 3) are remarkably similar in amplitude and in detailed space–time structure to the TMI SST observations. The RTG_SST analyses reproduce the cusplike undulating structure of the SST fronts with greater fidelity than do the Reynolds SST analyses (left panels in Fig. 6). It is apparent from the right panels in Fig. 6, however, that the SST gradients are significantly underestimated in the RTG_SST analyses.

The differences between the resolutions of the TMI, RTG_SST, and Reynolds SST fields are quantified by the histograms of SST gradient magnitudes computed for the time period August–December 2001 over the region north of the cold tongue where the SST gradients are strongest (Fig. 7). The distribution of SST gradients in the TMI fields is seen to be broad, with SST gradients that sometimes exceeded 3°C $(100\ \text{km})^{-1}$. In contrast, the dynamic range of SST gradients in the Reynolds SST analyses is narrow and SST gradients rarely exceeded 2°C $(100\ \text{km})^{-1}$. The breadth of the SST gradient distribution for the RTG_SST fields lies approximately halfway between those of the TMI and Reynolds distributions.

The temporal characteristics of SST variability in the three datasets are quantified by the time-lagged autocorrelations shown in the top panel in Fig. 8. The autocorrelations are almost identical for the 8-day loess-smoothed TMI and RTG_SST datasets. The damped cosine character and 8-day zero crossing are indicative of a dominant periodicity of about 16 days in SST variability within the region considered here. This dominant time scale is not dependent on the temporal smoothing since the zero crossing is unchanged in au-

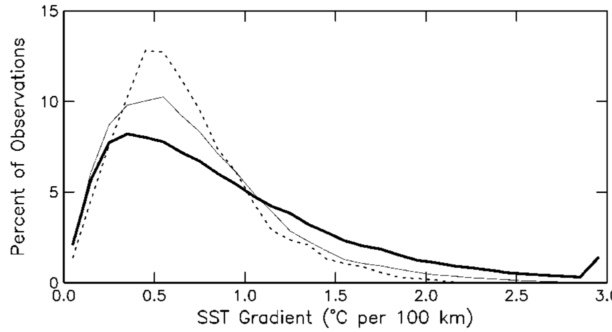


FIG. 7. Histograms of the SST gradient magnitude fields from TMI (heavy solid line), RTG_SST analyses (thin solid line), and Reynolds analyses (dashed line). As in Fig. 6, the TMI and RTG_SST fields were averaged over 3 days and smoothed spatially with a 2° × 2° loess smoother. No smoothing was applied to the 7-day average Reynolds analyses. The bin width of the histograms is 0.1°C $(100\ \text{km})^{-1}$ and the statistics were computed over the region on the north side of the cold tongue between the equator and 5°N and from 140° to 95°W from all of the 3-day or 7-day averages during the Aug–Dec 2001 cold season.

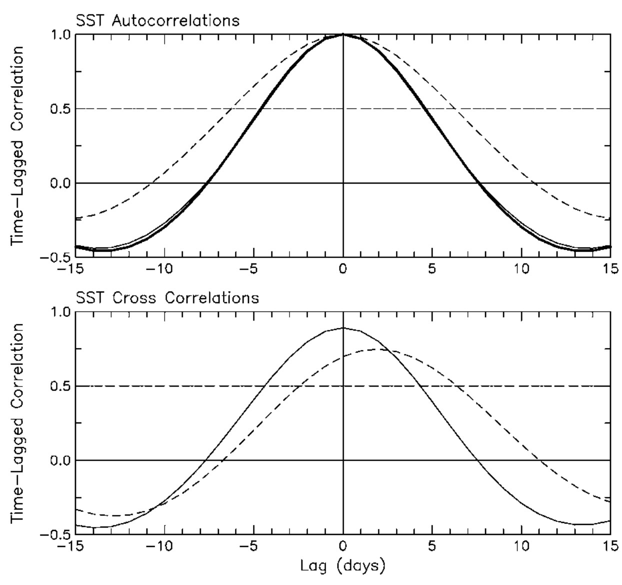


FIG. 8. Time-lagged correlation functions for the three zonal high-pass-filtered SST datasets analyzed in this study computed over the region 5°S–5°N, 140°–95°W and for the Aug–Dec 2001 cold season. (top) The heavy solid, thin solid, and dashed lines correspond, respectively, to the autocorrelations computed from TMI, RTG_SST, and Reynolds SST fields. (bottom) The thin solid and dashed lines correspond to the cross correlations of TMI with RTG_SST and Reynolds SST, respectively. Positive lags in the bottom panel correspond to RTG_SST and Reynolds lagging TMI. The SST fields from which these correlations were computed were processed as described in section 3c.

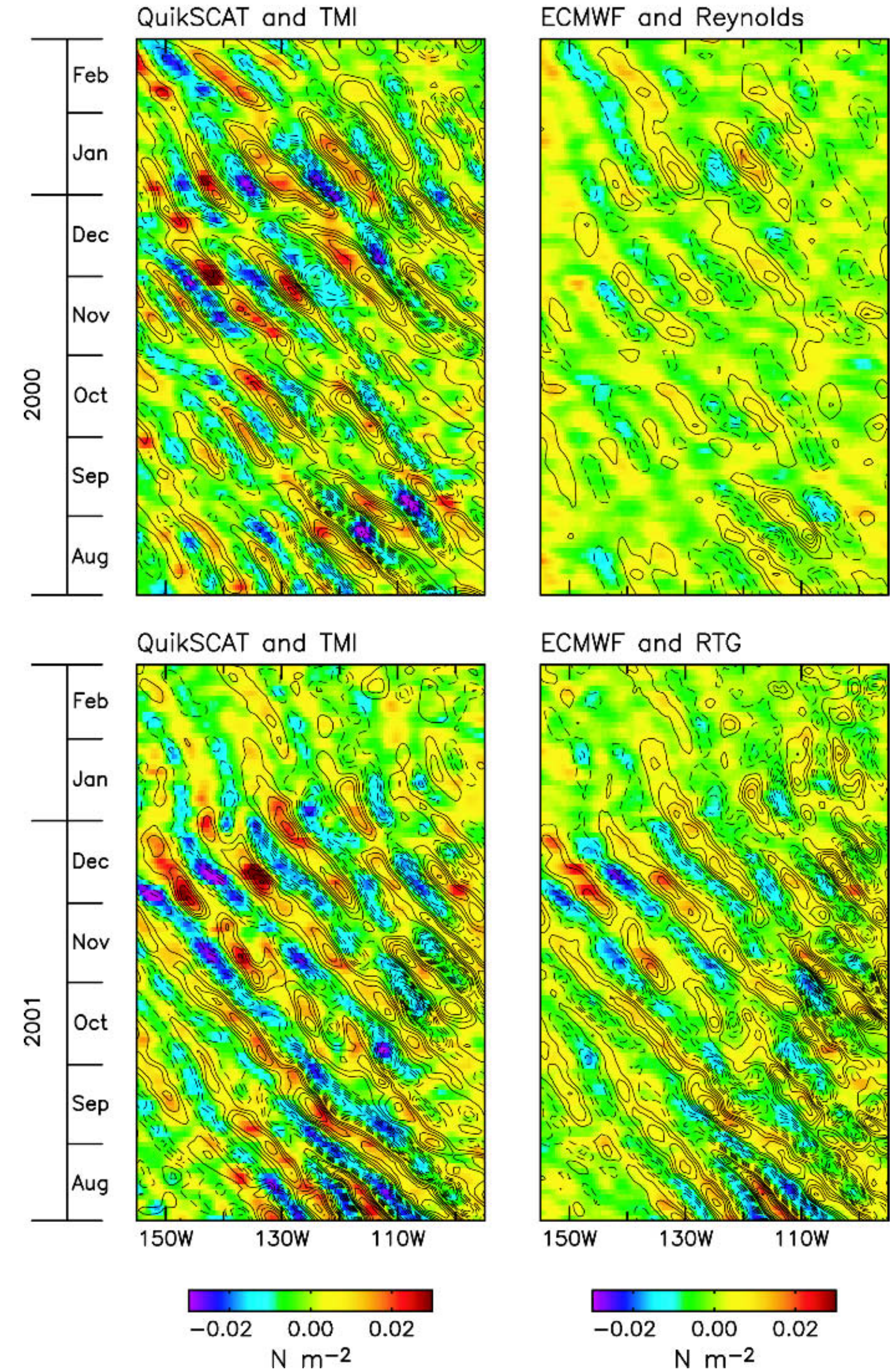


FIG. 9a. Time–longitude plots of zonal high-pass-filtered fields of wind stress magnitude (color) and SST (contours) along 2°N for the (top) 2000 and (bottom) 2001 cold seasons. (left) The QuikSCAT and TMI fields. (right) The ECMWF and (top) Reynolds and (bottom) RTG_SST fields. The SST contour interval is 0.25°C in all panels and the zero contours have been omitted for clarity.

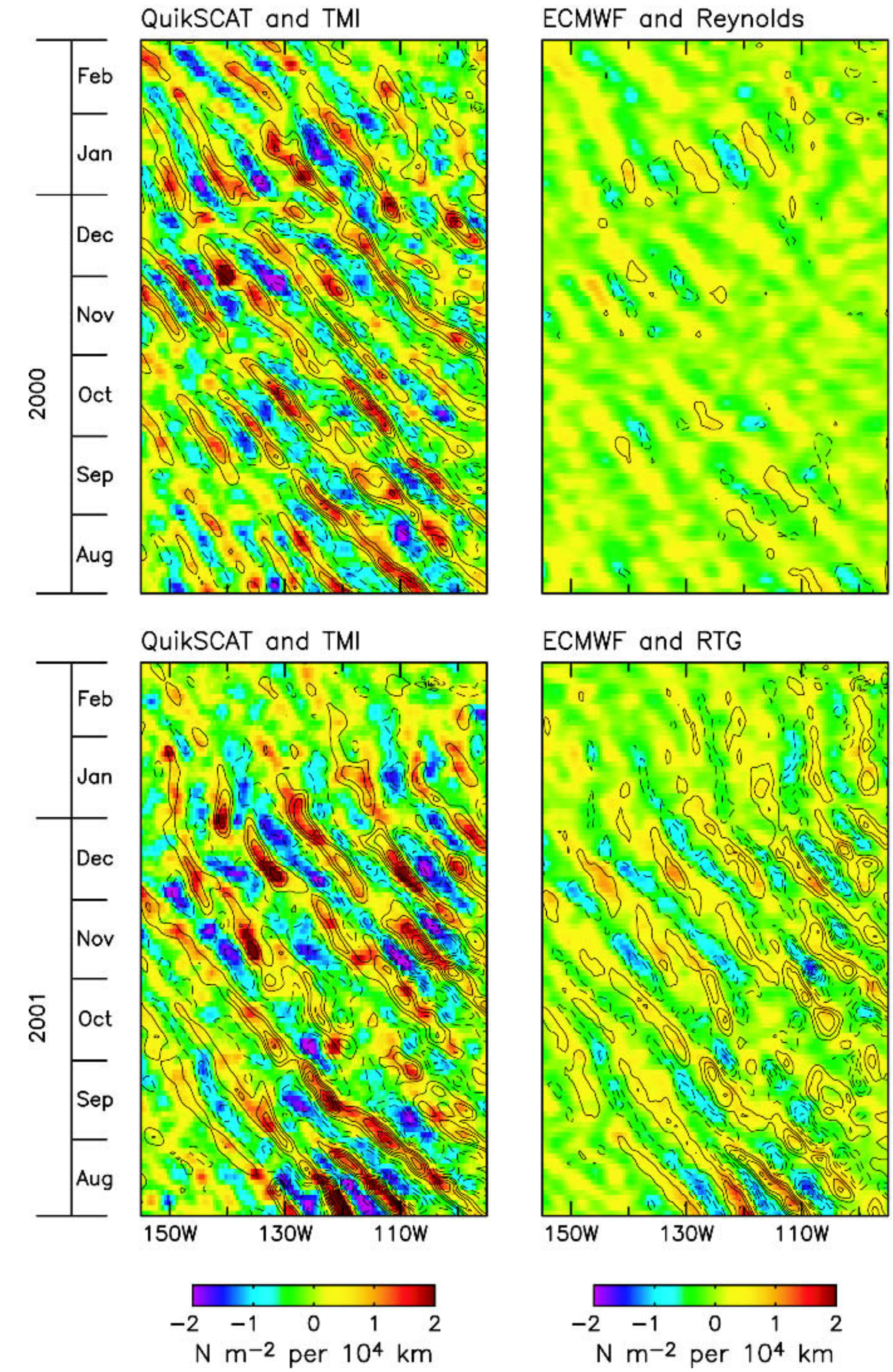


FIG. 9b. As in Fig. 9a except of wind stress divergence (color) and downwind SST gradient (contours) along 2°N. The downwind SST gradient contour interval is 0.25°C (100 km)$^{-1}$ in all panels and the zero contours have been omitted for clarity.

tocorrelations computed from daily average data. The 8-day zero crossing is therefore not imposed by the 8-day loess filtering applied to the TMI and RTG_SST data.

Variability in the Reynolds SST fields is more persistent than in the TMI and RTG_SST fields, with a zero crossing of the autocorrelation at about 11 days. The 7-day averaging in the Reynolds analyses is not a

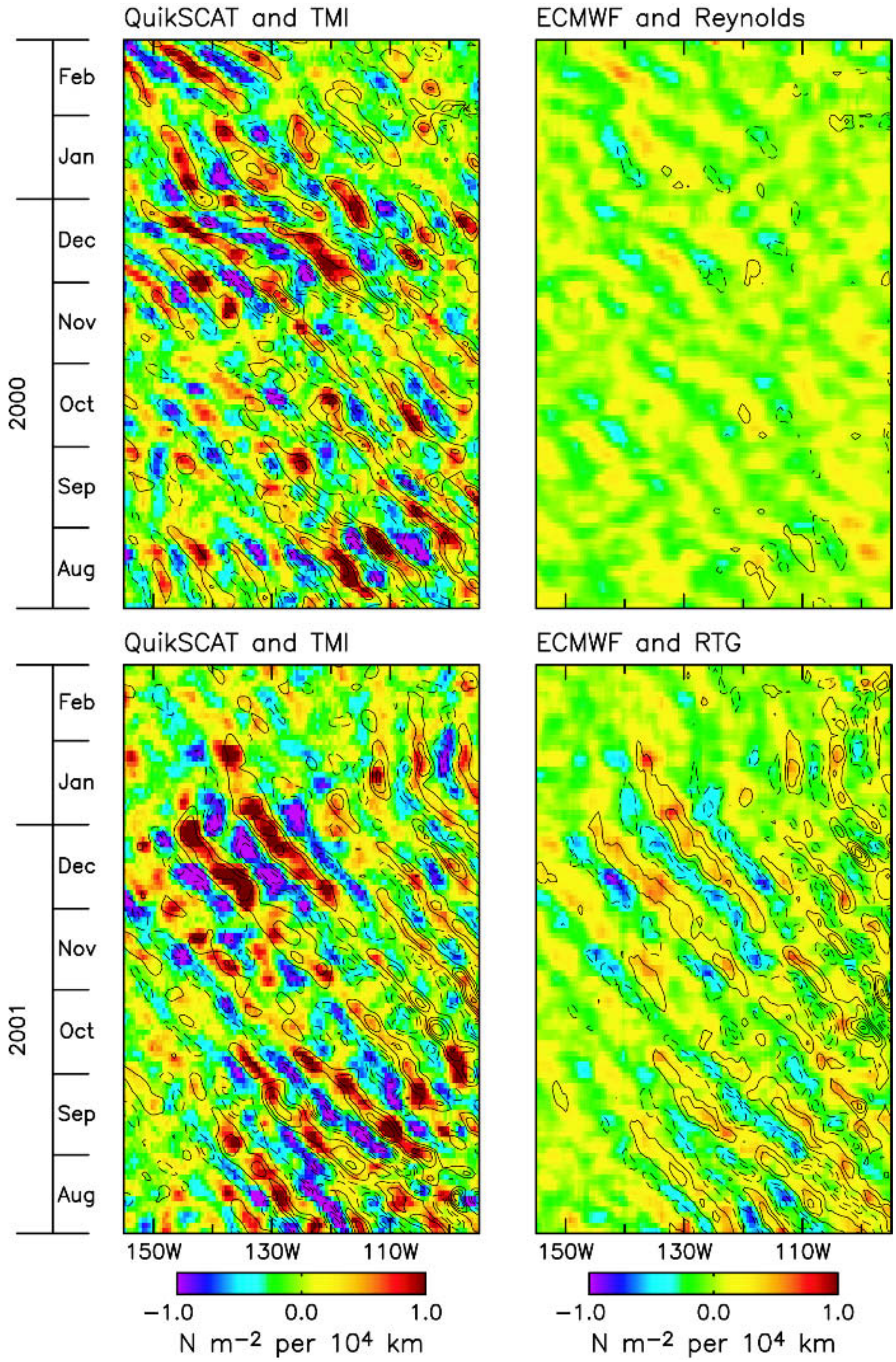


FIG. 9c. As in Fig. 9a except of wind stress curl (color) and crosswind SST gradient (contours) along 0.5°N. The crosswind SST gradient contour interval is 0.25°C (100 km)$^{-1}$ in all panels and the zero contours have been omitted for clarity.

major factor in this greater persistence since the dominant periodicity of about 16 days inferred from the TMI and RTG_SST data should be resolvable with the 12-day half-power point of 7-day averages. The greater persistence of the Reynolds SST analyses may be due to the fact that each 7-day-averaged SST analysis is based on a first guess that consists of the previous 7-day-averaged SST analysis.

The time-lagged cross correlations between TMI and the RTG_SST and Reynolds SST fields are shown in the bottom panel in Fig. 8. The maximum correlation between TMI and RTG_SST is 0.89 at zero lag. The maximum correlation between TMI and Reynolds is 0.75 at a lag of 2–3 days with the sign of the lag corresponding to Reynolds lagging TMI. The lag of maximum correlation apparently varies geographically for the Reynolds SST fields in the eastern tropical Pacific; the lag of maximum correlation with the four Tropical Atmosphere–Ocean (TAO) moorings (McPhaden et al. 1998) for which sufficiently gap-free data records exist within the study region during August–December 2001 varied from mooring to mooring, ranging from −1 day to +2 days. In contrast, the maximum correlations between the TAO moorings and both TMI and RTG_SST occurred at zero lag at all four moorings.

Although the 7-day-averaged Reynolds SST fields were never intended to be linearly interpolated to daily intervals for analysis in the manner in which they have been analyzed here, the bottom panel in Fig. 8 suggests that the centroid of each weekly average is shifted 2–3 days toward the beginning of the week, on average. The reason for this timing offset, which may be specific to the region considered here, is not yet known. It may be related to the tendency toward persistence imposed by using the previous SST analysis as the first guess for each new weekly average SST analysis.

It can be concluded from Figs. 6–8 that the RTG_SST analyses are a significant improvement over the Reynolds SST analyses in the eastern tropical Pacific region considered here. The conservatively long correlation length scales and 7-day averaging in the Reynolds analysis procedure are evidently not essential for SST analyses in this particular region.

While the resolution of the RTG_SST fields is higher than that of the Reynolds SST fields, it is important to note that inadequacies still exist in the RTG_SST fields. In particular, the intensities of the SST fronts as represented in the TMI observations are underestimated in the RTG_SST analyses (Figs. 6 and 7). The SST-induced perturbations of the wind stress field will therefore be underestimated in the ECMWF model, even if the boundary layer dynamics and thermodynamics of this ocean–atmosphere interaction process are both perfectly represented in the model.

## 5. Wind stress response to SST

The response of low-level winds to SST variations is evident from the time–longitude plots of zonal high-pass-filtered QuikSCAT and TMI data in the left panels in Figs. 9a,b,c. Perturbations of the wind stress magnitude (Fig. 9a), divergence (Fig. 9b), and curl (Fig. 9c) propagate synchronously westward with TIW-induced perturbations of the SST, downwind SST gradient, and crosswind SST gradient, respectively. The detailed space–time evolution of the relevant aspect of the SST field (the contours in each of the figures, as defined in the figure captions) is faithfully reproduced in each of these three characterizations of the wind stress field. The similarities of the histograms of QuikSCAT perturbation wind stress magnitude, divergence, and curl on the north side of the cold tongue for the two time periods (heavy solid and dashed lines in Fig. 10) are evidence of the similarity of oceanographic and meteorological conditions during the 2000 and 2001 cold seasons considered here.

The response of ECMWF winds to TIW-induced SST perturbations prior to 9 May 2001 should have lagged reality by about 4 days, on average, because of the time stamps on the daily updates of the Reynolds weekly average SST fields (see section 3b) used as the boundary condition in the ECMWF model. An additional lag of about 2 days can be expected because of the lag between the Reynolds SST analyses and reality (bottom panel in Fig. 8) that was speculated in section 4 to be due to persistence imposed by the first-guess SST

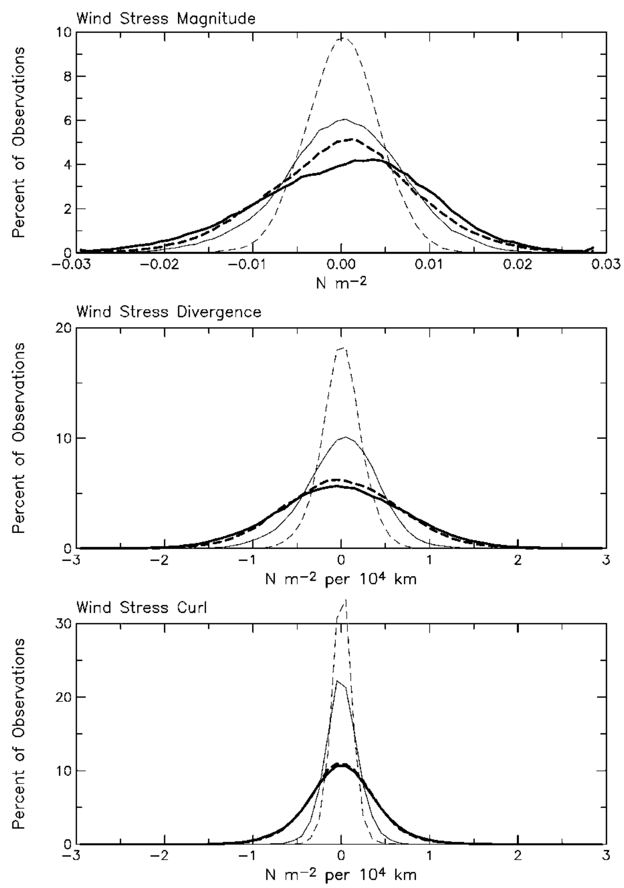


FIG. 10. Histograms of zonal high-pass-filtered fields of (top) wind stress magnitude, (middle) wind stress divergence, and (bottom) wind stress curl computed from QuikSCAT observations (heavy lines) and ECMWF wind stress fields (thin lines). Dashed and solid lines correspond to the 2000 and 2001 cold seasons, respectively. The bin sizes are (top) 0.001 N m$^{-2}$ and (middle), (bottom) 0.1 N m$^{-2}$ ($10^4$ km)$^{-1}$, and the statistics were computed over the region on the north side of the cold tongue between the equator and 5°N and from 140° to 95°W.

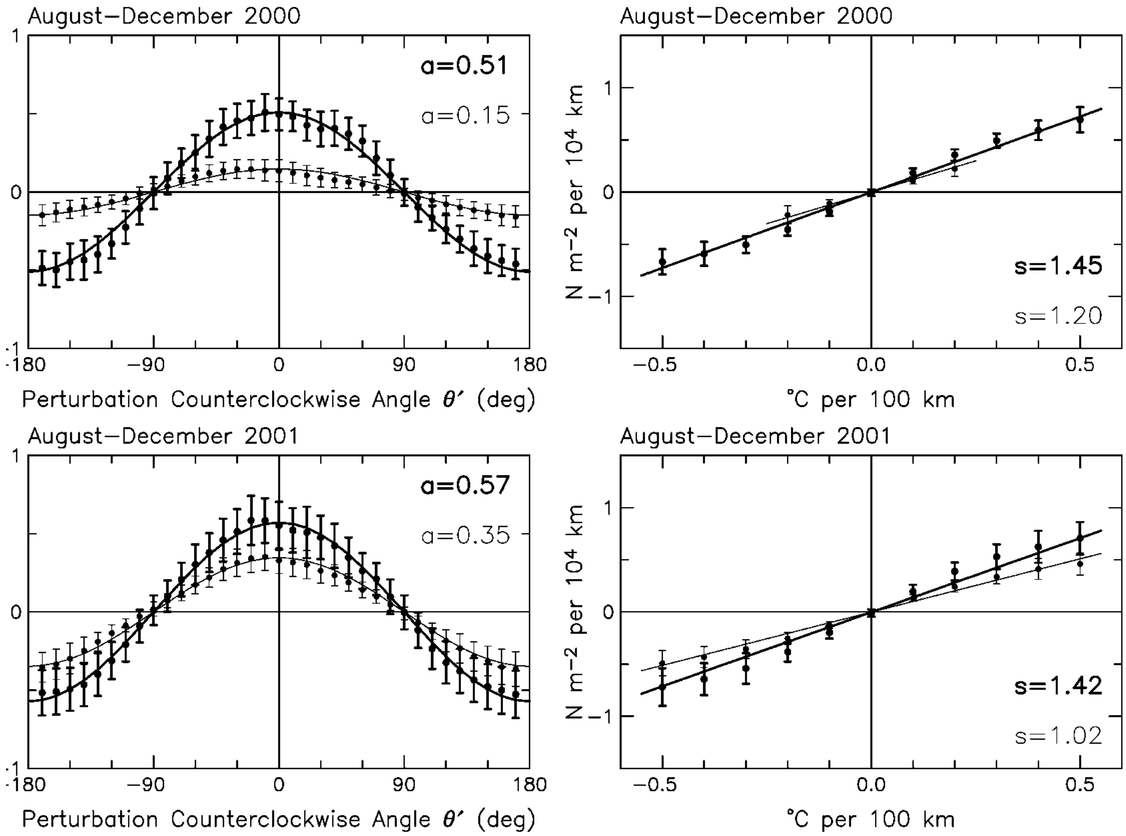


FIG. 11. Binned scatterplots of (left) the dependence of zonal high-pass-filtered wind stress divergence on the angle between the SST gradient vector and the wind direction and (right) the relationship between zonal high-pass-filtered wind stress divergence and the zonal high-pass-filtered downwind component of the SST gradient computed over the region 5°S–5°N, 140°–95°W. Results are shown for the (top) 2000 and (bottom) 2001 cold seasons. The thick lines are the results obtained from QuikSCAT and TMI observations and the thin lines are the results obtained from ECMWF and the (top) Reynolds and (bottom) RTG_SST fields. The parameters *a* are the amplitudes of the least squares fit cosines. The parameters *s* are the slopes of the least squares fit lines. The error bars in all plots represent the std devs of the scatter within each bin obtained from the smoothed and filtered fields over each 5-month cold season. (The dynamic range of the Reynolds downwind SST gradient in the upper-right panel is narrow because of the smoothness of the Reynolds SST fields; there were few perturbation downwind SST gradients with magnitudes larger than 0.2°C (100 km)$^{-1}$ for the 2000 analysis of the ECMWF wind stress divergence coupling with the SST field.)

fields in the Reynolds analyses. To account for these two sources of time lag, the ECMWF wind stress fields during the 2000 cold season were adjusted 6 days backward in time for comparisons with the Reynolds SST analyses in this section.

After 9 May 2001, the response of ECMWF winds to SST should have lagged reality by about a day, on average, because of the time stamps on the RTG_SST fields (see section 3b) used as the boundary condition in the ECMWF model since that time. No additional lag is expected since there is no lag between the RTG_SST and TMI SST fields (bottom panel in Fig. 8). The ECMWF fields during the 2001 cold season were therefore adjusted 1 day backward in time for comparisons with the RTG_SST analyses in this section.

Synchrony with the SST signatures of westward-propagating TIWs is qualitatively evident in the time-adjusted ECMWF perturbation wind stress fields (right panels in Figs. 9a,b,c), albeit with considerably smaller amplitudes than the perturbation wind stress magnitude, divergence, and curl computed from QuikSCAT observations. The amplitudes of the perturbation wind stress fields were especially weak during the 2000 time period in which the surface boundary condition in the ECMWF model consisted of the Reynolds SST analyses.

The weaker perturbations in the ECMWF wind stress fields are quantified by the histograms in Fig. 10. Compared with the distributions in the QuikSCAT observations, the dynamic ranges of the ECMWF wind stress magnitude, divergence, and curl on the north side of the cold tongue where the ocean–atmosphere interaction is strongest were less than 50% as large during the 2000 cold season and only about 75% as large during the 2001 cold season. These decreases are roughly in proportion to the decreases in the dynamic ranges of the Reynolds and RTG_SST gradient magnitudes in comparison with the dynamic range of the TMI SST gradient magnitudes (Fig. 7). This sensitivity to the

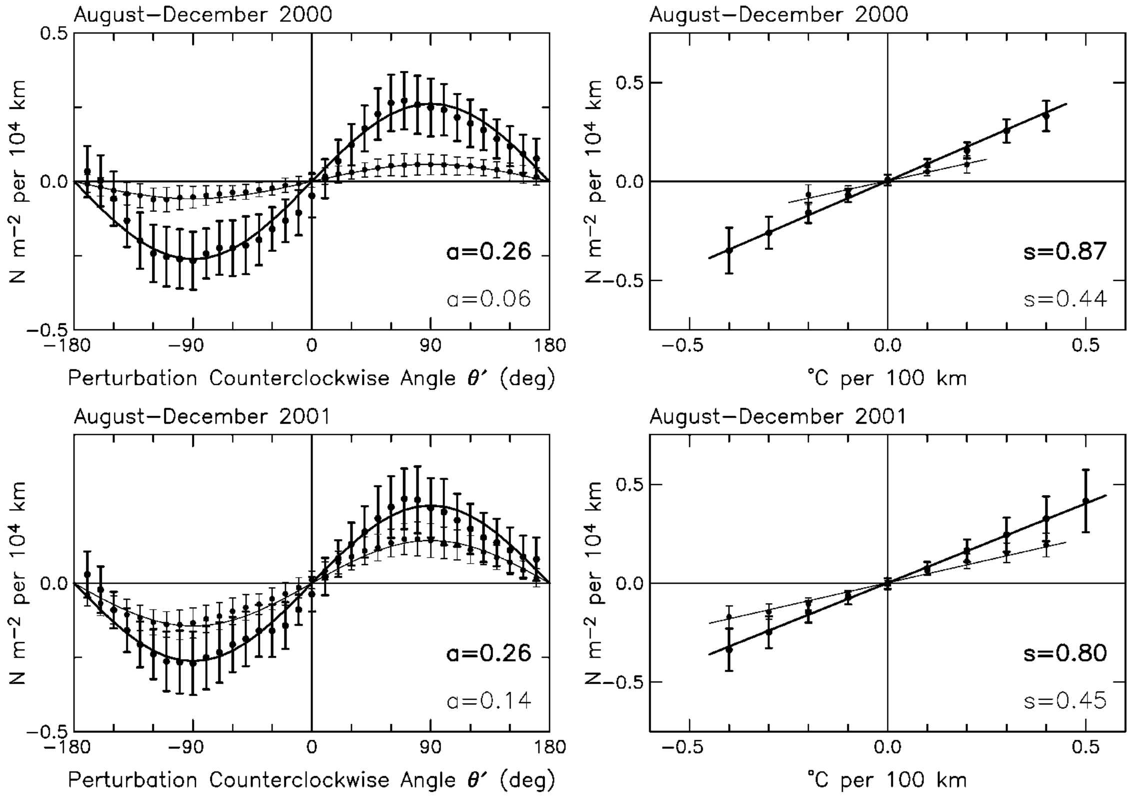


FIG. 12. As in Fig. 11 except binned scatterplots of (left) the dependence of zonal high-pass-filtered wind stress curl on the angle between the SST gradient vector and the wind direction and (right) the relationship between zonal high-pass-filtered wind stress curl and the zonal high-pass-filtered crosswind component of the SST gradient.

magnitudes of the SST gradients indicates that the weaker response of the ECMWF wind stress fields to SST variability is at least partly attributable to the weaker small-scale SST gradients in the ocean boundary condition.

The effects of SST on the wind stress divergence are quantified in Fig. 11. The binned averages in the left panels indicate that the perturbation divergence varies as the cosine of the angle between the perturbation wind stress vector and the perturbation SST gradient vector. This cosine dependence implies that the divergence is related to the downwind component of the SST gradient, as expected from the schematic summary in Fig. 4 and the observational results obtained previously by Chelton et al. (2001). The amplitudes $a$ of the cosine fits to the QuikSCAT and TMI data, which represent the average divergence response to SST when the wind blows parallel to the SST gradient vector, differ by only about 12% for 2000 and 2001, again indicating that the oceanographic and meteorological conditions were similar during the two cold seasons considered here.

From the cosine fits to the 2000 and 2001 ECMWF wind stress divergence fields, it is apparent that the amplitudes of the ECMWF wind stress divergence perturbations were more than twice as large in 2001 as in 2000. Although a significant improvement, the amplitudes of the SST-induced perturbations of the ECMWF wind stress divergence field in 2001 after changing to the RTG_SST boundary condition were still only about 60% as large as the QuikSCAT wind stress divergence perturbations.

The linear relationship between the wind stress divergence and the downwind component of the SST gradient is evident from the binned averages in the right panels in Fig. 11. The coupling coefficients $s$ from the QuikSCAT and TMI data are almost identical for the 2000 and 2001 cold seasons considered here, and are nearly the same as the value obtained for the cold season of 1999 by Chelton et al. (2001) for the region on the north side of the equatorial cold tongue.[3] The coupling coefficients for the ECMWF wind stress di-

[3] The responses of divergence and curl to the downwind and crosswind SST gradients are about twice as strong on the south side of the cold tongue as on the north side (Chelton et al. 2001). This is presumably attributable to differences in the detailed structures of the marine atmospheric boundary layer north and south of the cold tongue. Because of the greater dynamic range of SST gradients on the north side (see, e.g., Plates 3 and 4 of Chelton et al. 2000) owing to the stronger SST front, the statistics of the wind stress divergence and curl responses to SST obtained here for the region 5°S–5°N are dominated by conditions on the north side of the cold tongue.

vergence were significantly smaller than those for the QuikSCAT divergence. A given downwind SST gradient therefore generates a weaker response of the wind stress divergence. This indicates that the boundary layer processes by which the wind field is modified by spatial variations in the SST are underrepresented in the ECMWF model.

While the coupling coefficient for the ECMWF model was about 20% smaller in 2001 than in 2000 (probably not a statistically significant difference given the narrow dynamic range of the downwind SST gradient in the Reynolds SST fields and, therefore, in the wind stress divergence fields during the 2000 time period), the amplitude of the cosine fit in the left panels was more than a factor of 2 larger in 2001. This increase must be due to the stronger SST gradients in the RTG_SST analyses compared with the Reynolds SST analyses since the coupling coefficients suggest that, if anything, the boundary layer processes were slightly less strongly represented in the ECMWF model during 2001.

It is thus apparent that the smaller amplitudes of the ECMWF wind stress divergence perturbations in Fig. 9b are attributable partly to a weaker coupling between wind stress and SST in the ECMWF model and partly to the lower resolution (weaker gradients) of the SST fields used as the ECMWF ocean boundary condition.

The effects of the SST field on the wind stress curl are summarized in Fig. 12. Consistent with the schematic summary in Fig. 4 and the observational results obtained previously by Chelton et al. (2001), the binned averages in the left panels indicate that the curl varies as the sine of the angle between the perturbation wind stress vector and the perturbation SST gradient vector. The curl is thus related to the crosswind component of the SST gradient. The amplitudes $a$ of the sine fits to the QuikSCAT and TMI data, which represent the average curl response to SST when the wind blows perpendicular to the SST gradient vector, are the same in both years. The amplitudes of the sine fits to the binned averages of the ECMWF wind stress curl are even smaller relative to the QuikSCAT results than was the case for the ECMWF wind stress divergence fields in Fig. 11. This discrepancy may be due to small but systematic directional errors in the ECMWF wind fields that orient the winds relative to the SST front more favorably for the development of divergence than for curl.

The linear relationship between the wind stress curl and the crosswind component of the SST gradient is shown in the right panels in Fig. 12. The coupling coefficients $s$ from the QuikSCAT and TMI data differ by less than 10% for the cold seasons of 2000 and 2001 and are nearly the same as the value obtained for the cold season of 1999 by Chelton et al. (2001) for the region on the north side of the equatorial cold tongue. In comparison, the coupling coefficients for the ECMWF wind stress curl are only about half as large, differing from the QuikSCAT coupling coefficients by more than was the case for the wind stress divergence. A given crosswind SST gradient therefore generates a weaker response of the wind stress curl, again indicating that the boundary layer processes are underrepresented in the ECMWF model.

While the coupling coefficients for the ECMWF wind stress curl were virtually identical for both years, the amplitude of the sine fit in the left panels was more than a factor of 2 larger in 2001 than in 2000. As in the stronger response of the ECMWF wind stress divergence during 2001, this increase must be attributable to the stronger SST gradients in the RTG_SST analyses compared with the Reynolds SST analyses, again indicating the importance of resolution in the SST boundary condition.

Specification of the SST boundary condition thus has a clear impact on the ECMWF wind stress field. The approximate factor of 2 stronger perturbations of the ECMWF wind stress divergence and curl in 2001 compared with 2000 is a measure of the positive impact of the higher spatial and temporal resolution of the RTG_SST analyses compared with the Reynolds SST analyses. Though a significant improvement, the SST-induced perturbations in the 2001 ECMWF wind stress

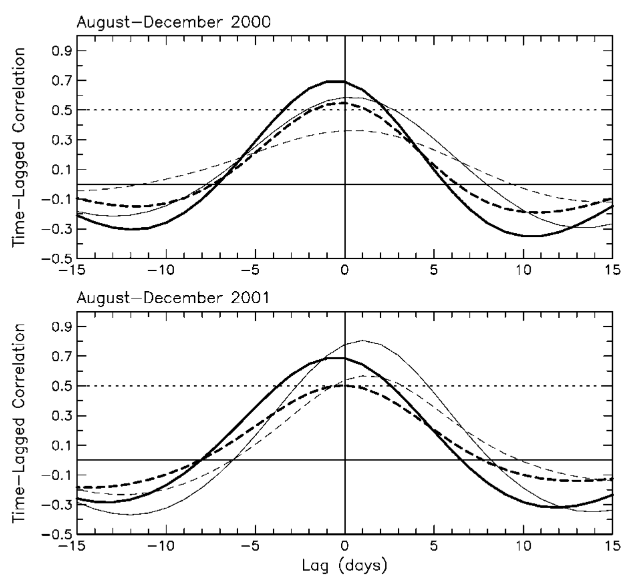


Fig. 13. Time-lagged cross-correlations between zonal high-pass-filtered derivative wind stress fields and the zonal high-pass-filtered SST gradient component fields for the (top) 2000 and (bottom) 2001 cold seasons computed over the region 5°S–5°N, 140°–95°W. Heavy lines correspond to correlations based on QuikSCAT and TMI observations and thin lines correspond to correlations based on ECMWF wind stress fields and the (top) Reynolds and (bottom) RTG_SST analyses. Solid lines are the correlations between the wind stress divergence and the downwind SST gradient and dashed lines are the correlations between the wind stress curl and the crosswind SST gradient. Positive lags correspond to winds lagging SST.

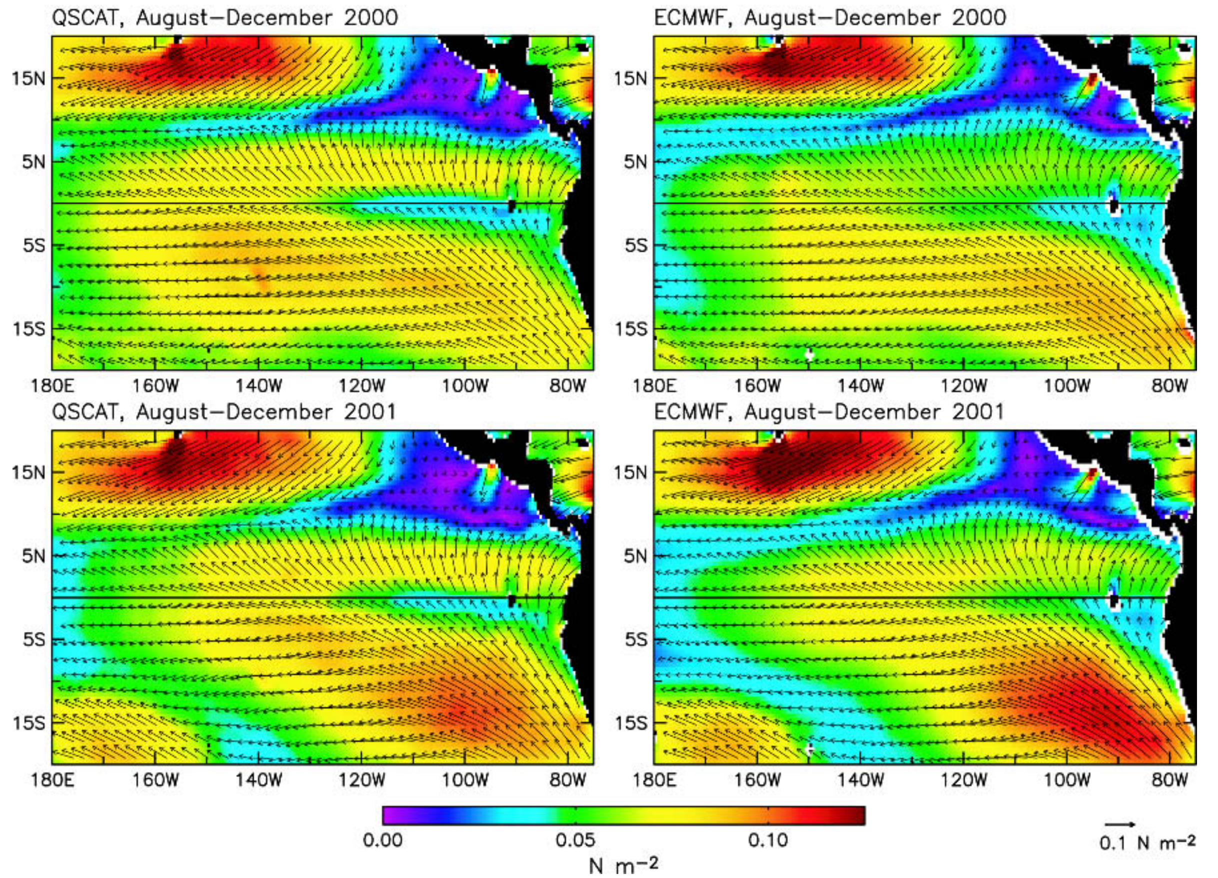


FIG. 14a. Five-month vector averages of (left) QuikSCAT and (right) ECMWF wind stress fields for the Aug–Dec cold seasons of (top) 2000 and (bottom) 2001. For clarity, vectors are displayed on a 2° latitude by 2° longitude grid. The magnitude of the vector-average wind stress is represented in color according to the scale indicated on the color bar.

fields were still only about half as large as in the QuikSCAT wind stress fields. As summarized above, this is attributable partly to underestimates of the SST gradients in the RTG_SST fields and partly to weaker coupling coefficients for the ECMWF wind stress divergence and curl responses to the downwind and crosswind SST gradients. The latter are indicative of inadequacies of the ECMWF model, either from errors in the parameterization of the boundary layer processes or to insufficient vertical or horizontal resolution in the model.

The time-lagged correlations between the derivative wind stress fields (divergence and curl) and the associated SST gradient components (downwind and crosswind, respectively) shown in Fig. 13 reveal a puzzling aspect of the ocean–atmosphere coupling in the ECMWF wind stress fields during the 2001 cold season. Even after the 1-day time adjustment applied here, as noted previously, the perturbations of divergence and curl in the 2001 ECMWF wind stress fields both lag the perturbation downwind and crosswind SST gradients in the RTG_SST fields by about a day. No such lag is evident in either the 2000 ECMWF wind stress fields (after the 6-day time adjustment applied here) or the QuikSCAT wind stress fields.[4] The reason for the additional lag in the 2001 ECMWF wind stress fields is not presently known. It is also curious that the correlations between the derivative wind stress fields and the SST gradient components were actually larger for the 2001 ECMWF and RTG_SST fields than for the QuikSCAT and TMI fields.

## 6. Discussion and conclusions

Ocean–atmosphere coupling in the eastern tropical Pacific was examined from 8-day smoothed wind stress

[4] The asymmetry in the lagged correlations for the QuikSCAT wind stress fields for both 2000 and 2001 suggests that the divergence and curl were both more highly correlated with later SST perturbations than with earlier SST perturbations. This nonphysical apparent relation was determined to be attributable to asymmetry in the spatial lagged correlation that masquerades as an asymmetry in the time-lagged correlation because of the systematic westward propagation of the SST and wind stress perturbations in this region.

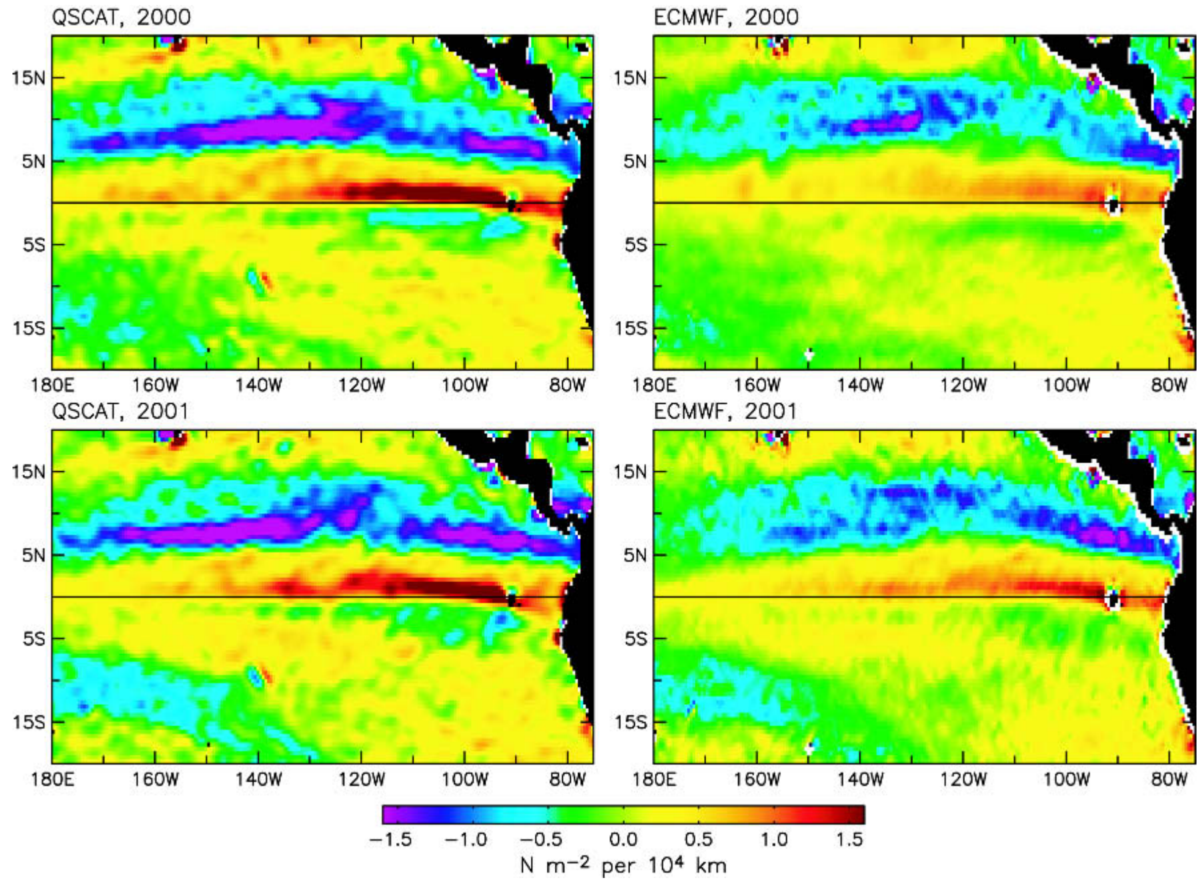


FIG. 14b. As in Fig. 14a except the 5-month averages of wind stress divergence.

and SST fields. The strong coupling previously identified from QuikSCAT and TMI observations of wind stress and SST during the 1999 cold season (Chelton et al. 2001) was verified for the 2000 and 2001 cold seasons. This coupling is most clearly manifest in the divergence and curl of the wind stress fields, which are linearly related respectively to the downwind and crosswind components of the SST gradient.

The same ocean–atmosphere coupling is evident in the ECMWF wind stress fields. The sensitivity of ECMWF wind stress fields to specification of the SST boundary condition was unequivocally demonstrated in the eastern tropical Pacific from an examination of ECMWF winds before and after the 9 May 2001 change from the Reynolds SST analyses to the RTG_SST analyses as the ocean boundary condition for the ECMWF model. Consistent with the QuikSCAT and TMI observations, the ECMWF wind stress fields respond rapidly to spatial and temporal variations in the underlying SST field. Because of their higher spatial and temporal resolution, the SST gradients are stronger in the RTG_SST fields than in the Reynolds analyses. This difference in the SST boundary condition is manifest in the ECMWF model as about a factor-of-2 increase in the amplitudes of SST-induced perturbations of the wind stress field during the 2001 cold season compared with the 2000 cold season.

Because the time stamps for the daily updates of the Reynolds 7-day-averaged SST analyses and the daily updates of the RTG_SST daily average SST analyses correspond to the end of each analysis period and because the ECMWF model used a constant SST boundary condition for 24 h until the next daily update of SST is available, the ECMWF wind stress fields unavoidably lagged reality by about 4 days before 9 May 2001 and by about 1 day after 9 May 2001. Additional lags were deduced from the analysis presented here. In the case of the 2000 ECMWF wind stress fields, an additional lag of about 2 days is attributable to an approximate 2-day lag in the centroid of the Reynolds analyses of weekly average SST in this region, evidently due to a tendency for persistence in the Reynolds SST analyses. In the case of the 2001 ECMWF analyses, there was an additional lag of about 1 day for unknown reasons.

In total, the ECMWF perturbation wind stress fields in the eastern tropical Pacific region considered here thus lagged reality by about 6 days during the 2000 cold season when the ocean boundary condition consisted of the Reynolds SST analyses. Because of the approximate monthly periodicity of TIWs, the SST-induced

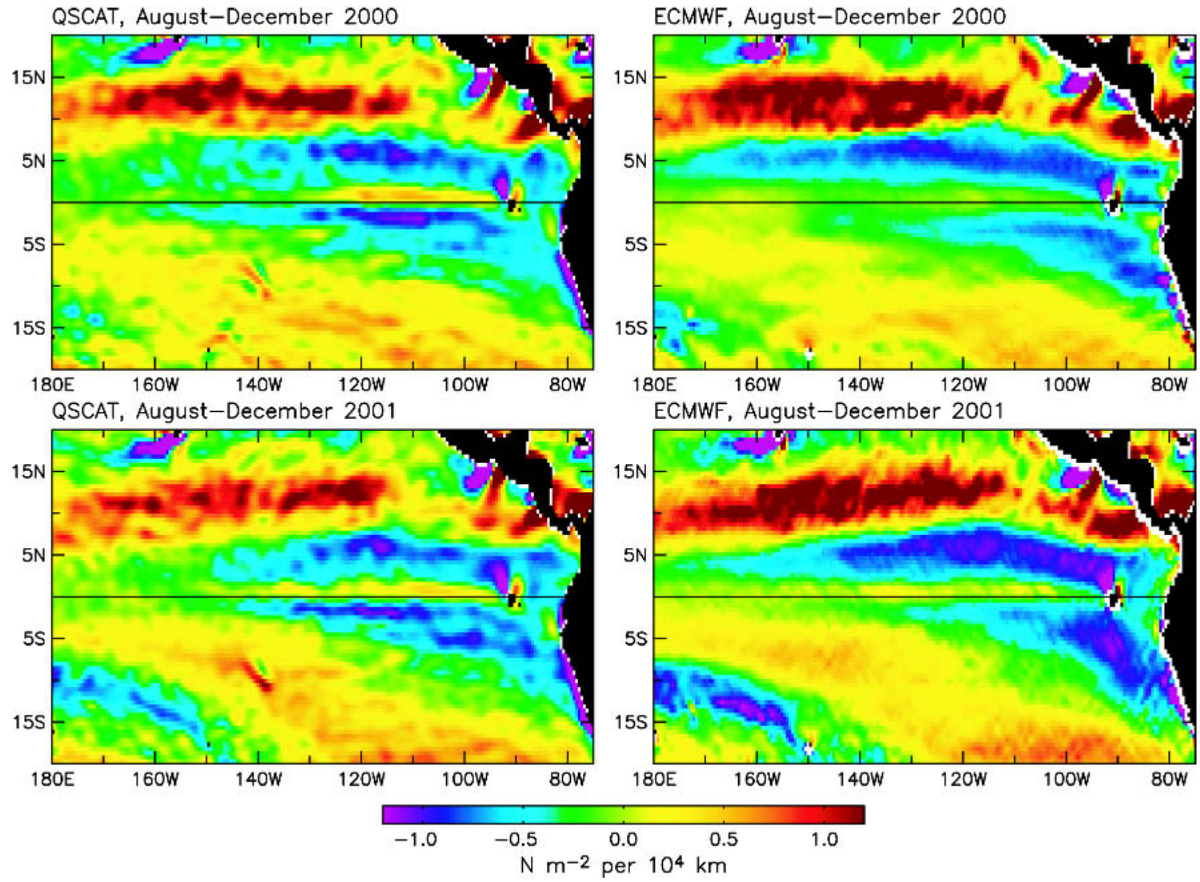


FIG. 14c. As in Fig. 14a except the 5-month averages of wind stress curl.

perturbations of the ECMWF wind stress fields prior to May 2001 were roughly in quadrature with reality. After the boundary condition was changed to the RTG_SST analyses on 9 May 2001, the ECMWF wind stress fields lagged reality by about 2 days.

While a significant improvement compared with 2000, the amplitudes of the SST-induced perturbations of the wind stress fields were still underestimated by about a factor of 2 in the 2001 ECMWF wind stress fields. It was shown that this can be attributed partly to underrepresentation of SST gradients in the RTG_SST fields and partly to underrepresentation of the ocean–atmosphere coupling in the ECMWF model (i.e., the smaller magnitudes of the coupling coefficients in the right panels in Figs. 11 and 12). The latter may be due to the poor vertical resolution of the ECMWF model within the marine atmospheric boundary layer and to errors in the model parameterization of turbulent mixing. The underrepresentation of ocean–atmosphere coupling may also be due to the coarse horizontal resolution of the ECMWF wind stress fields; although the grid resolution of the ECMWF model was 0.564° during 2000 and 0.352° during 2001, the wind fields in present numerical weather prediction models are only able to resolve features with wavelength scales longer than about 500 km (e.g., Milliff et al. 2004).

The underrepresentation of ocean–atmosphere coupling in the ECMWF wind stress fields has important implications for ocean models that are forced by the ECMWF wind stress fields. The geographical variability of the climatological average wind stress field in the vicinity of the equatorial cold tongue is much weaker than in the QuikSCAT wind stress fields. This is evident from the 5-month vector average wind stress and scalar average divergence and curl of the wind stress shown in Figs. 14a,b,c. [5] The underrepresentation of the influence of the cold tongue on the ECMWF wind stress fields, which is especially dramatic prior to the 9 May 2001 change to the RTG_SST boundary condition, likely has a significant effect on the simulated structure

[5] The anomalous features in the QuikSCAT wind stress fields near 10°S, 140°W that are especially clear in the divergence and curl fields in Figs. 14b and 14c are attributable to orographic effects of the Marquesas Islands. Such small-scale features are evident in the QuikSCAT data near many islands, but are not resolved in the wind stress fields from numerical weather prediction models (Chelton et al. 2004).

of the cold tongue and the accuracy of the tropical ocean circulation.

Improvements in the ECMWF model from more accurate specification of the SST boundary condition are thus important for modeling both the low-level atmosphere and the ocean. It is highly likely that the objective analysis systems for the Reynolds and RTG_SST analyses of global SST could benefit greatly from inclusion of all-weather satellite microwave measurements of SST from the TMI and the Advanced Microwave Scanning Radiometer (Wentz and Meissner 2000).

*Acknowledgments.* I thank Michael Schlax for data processing support and for detailed comments on the manuscript. I also thank Steve Esbensen, Eric Maloney, Ralph Milliff, Larry O'Neill, and Dick Reynolds for thorough comments on the manuscript, and Anton Beljaars, Hans Hersbach and Bert Katz for helpful discussions during the course of this research. This research was supported by NASA Grant NAS5-32965.

REFERENCES

Bond, N. A., 1992: Observations of planetary boundary-layer structure in the eastern equatorial Pacific. *J. Climate,* **5,** 699–706.

Chelton, D. B., and M. G. Schlax, 2003: The accuracies of smoothed sea surface height fields constructed from tandem altimeter datasets. *J. Atmos. Oceanic Technol.,* **20,** 1276–1302.

——, and M. H. Freilich, 2005: Scatterometer-based assessment of 10-m wind analyses from the operational ECMWF and NCEP numerical weather prediction models. *Mon. Wea. Rev.,* **133,** 409–429.

——, F. J. Wentz, C. L. Gentemann, R. A. de Szoeke, and M. G. Schlax, 2000: Microwave SST observations of transequatorial tropical instability waves. *Geophys. Res. Lett.,* **27,** 1239–1242.

——, and Coauthors, 2001: Observations of coupling between surface wind stress and sea surface temperature in the eastern tropical Pacific. *J. Climate,* **14,** 17 877–17 904.

——, M. G. Schlax, M. H. Freilich, and R. F. Milliff, 2004: Satellite measurements reveal persistent small-scale features in ocean winds. *Science,* **303,** 978–983.

Cleveland, W. S., and S. J. Devlin, 1988: Locally weighted regression: An approach to regression analysis by local fitting. *J. Amer. Stat. Assoc.,* **83,** 596–610.

Cronin, M. F., S.-P. Xie, and H. Hashizume, 2003: Barometric pressure variations associated with eastern Pacific tropical instability waves. *J. Climate,* **16,** 3050–3057.

Deser, C., J. J. Bates, and S. Wahl, 1993: The influence of sea surface temperature on stratiform cloudiness along the equatorial front in the Pacific Ocean. *J. Climate,* **6,** 1172–1180.

de Szoeke, S. P., and C. S. Bretherton, 2004: Quasi-Lagrangian large eddy simulations of cross-equatorial flow in the east Pacific atmospheric boundary layer. *J. Atmos. Sci.,* **61,** 1837–1858.

Gentemann, C. L., F. J. Wentz, C. A. Mears, and D. K. Smith, 2004: In situ validation of Tropical Rainfall Measuring Mission microwave sea surface temperatures. *J. Geophys. Res.,* **109,** C04021, doi:10.1029/2003JC002092.

Hashizume, H., S.-P. Xie, W. T. Liu, and K. Takeuchi, 2001: Local and remote atmospheric response to tropical instability waves: A global view from space. *J. Geophys. Res.,* **106,** 10 173–10 185.

——, ——, M. Fujiwara, M. Shiotani, T. Watanabe, Y. Tanimoto, W. T. Liu, and K. Takeuchi, 2002: Direct observations of atmospheric boundary layer response to slow SST variations over the eastern equatorial Pacific. *J. Climate,* **15,** 3379–3393.

Hayes, S. P., M. J. McPhaden, and J. M. Wallace, 1989: The influence of sea-surface temperature on surface wind in the eastern equatorial Pacific: Weekly to monthly variability. *J. Climate,* **2,** 1500–1506.

Jury, M. R., 1994: A thermal front within the marine atmospheric boundary layer over the Agulhas Current south of Africa: Composite aircraft observations. *J. Geophys. Res.,* **99,** 3297–3304.

——, and N. Walker, 1988: Marine boundary layer modification across the edge of the Agulhas Current. *J. Geophys. Res.,* **93,** 647–654.

Lindzen, R. S., and S. Nigam, 1987: On the role of sea surface temperature gradients in forcing low-level winds and convergence in the tropics. *J. Atmos. Sci.,* **44,** 2418–2436.

Liu, W. T., X. Xie, P. S. Polito, S.-P. Xie, and H. Hashizume, 2000: Atmospheric manifestation of tropical instability waves observed by QuikSCAT and Tropical Rain Measuring Mission. *Geophys. Res. Lett.,* **27,** 2545–2548.

McPhaden, M. J., and Coauthors, 1998: The Tropical Ocean–Global Atmosphere observing system: A decade of progress. *J. Geophys. Res.,* **103,** 14 169–14 240.

Mechoso, C. R., and Coauthors, 1995: The seasonal cycle over the tropical Pacific in coupled ocean–atmosphere general circulation models. *Mon. Wea. Rev.,* **123,** 2825–2838.

Milliff, R. F., J. Morzel, D. B. Chelton, and M. H. Freilich, 2004: Wind stress curl and wind stress divergence biases from rain effects on QSCAT surface wind retrievals. *J. Atmos. Oceanic Technol.,* **21,** 1216–1231.

O'Neill, L. W., D. B. Chelton, and S. K. Esbensen, 2003: Observations of SST-induced perturbations of the wind stress field over the Southern Ocean on seasonal time scales. *J. Climate,* **16,** 2340–2354.

Qiao, L., and R. H. Weisberg, 1995: Tropical instability wave kinematics: Observations from the Tropical Instability Wave Experiment. *J. Geophys. Res.,* **100,** 8677–8693.

Reynolds, R. W., and T. M. Smith, 1994: Improved global sea surface temperature analyses using optimum interpolation. *J. Climate,* **7,** 929–948.

——, N. A. Rayner, T. M. Smith, D. C. Stokes, and W. Wang, 2002: An improved in situ and satellite SST analysis for climate. *J. Climate,* **15,** 1609–1625.

Schlax, M. G., D. B. Chelton, and M. H. Freilich, 2001: Sampling errors in wind fields constructed from single and tandem scatterometer datasets. *J. Atmos. Oceanic Technol.,* **18,** 1014–1036.

Small, R. J., S.-P. Xie, and Y. Wang, 2003: Numerical simulation of atmospheric response to Pacific tropical instability waves. *J. Climate,* **16,** 3723–3741.

Sweet, W. R., R. Fett, J. Kerling, and P. LaViolette, 1981: Ocean–atmosphere interaction effects in the lower troposphere across the north wall of the Gulf Stream. *Mon. Wea. Rev.,* **109,** 1042–1052.

Thiébaux, J., E. Rogers, W. Wang, and B. Katz, 2003: A new high-resolution blended real-time global sea surface temperature analysis. *Bull. Amer. Meteor. Soc.,* **84,** 645–656.

Thum, N., S. K. Esbensen, D. B. Chelton, and M. J. McPhaden, 2002: Ocean–atmosphere heat exchange along the northern sea surface temperature front in the eastern tropical Pacific. *J. Climate,* **15,** 3361–3378.

Trenberth, K. E., W. G. Large, and J. G. Olson, 1990: The mean annual cycle in global ocean wind stress. *J. Phys. Oceanogr.,* **20,** 1742–1760.

Wallace, J. M., T. P. Mitchell, and C. Deser, 1989: The influence of sea surface temperature on surface wind in the eastern equatorial Pacific: Seasonal and interannual variability. *J. Climate,* **2,** 1492–1499.
Wentz, F. J., and T. Meissner, 2000: Algorithm Theoretical Basis Document (ATBD), version 2. AMSR Ocean Algorithm. Remote Sensing Systems Tech. Rep. RSS 121599A-1, 59 pp. [Available online at www.remss.com/papers/AMSR_Ocean_Algorithm_Version_2.doc.]
——, C. Gentemann, D. Smith, and D. Chelton, 2000: Satellite measurements of sea surface temperature through clouds. *Science,* **288,** 847–850.
Xie, S.-P., 2004: Satellite observations of cool ocean–atmosphere interaction. *Bull. Amer. Meteor. Soc.,* **85**, 195–209.
——, M. Ishiwatari, H. Hashizume, and K. Takeuchi, 1998: Coupled ocean-atmosphere waves on the equatorial front. *Geophys. Res. Lett.,* **25,** 3863–3866.
——, W. T. Liu, Q. Liu, and M. Nonaka, 2001: Far-reaching effects of the Hawiian Islands on the Pacific ocean-atmosphere system. *Science,* **292,** 2057–2060.